

Article

First-Principles Calculations of the Phonon, Mechanical and Thermoelectric Properties of Half-Heusler Alloy VIrSi Alloys

Paul O. Adebambo ^{1,*} , Bamidele I. Adetunji ², Oghenekevwe T. Uto ³ , Stephane Kenmoe ^{4,*} and Gboyega A. Adebayo ^{1,*} 

¹ Department of Physics, Federal University of Agriculture, Abeokuta P.M.B. 2240, Nigeria

² Department of Physics, Bells University of Technology, Ota 23401, Nigeria

³ Department of Physics, The University of the Gambia, Kanifing, Serrekunda P.O. Box 3530, The Gambia

⁴ Department of Theoretical Chemistry, University of Duisburg-Essen, Universitätsstr. 2, D-45141 Essen, Germany

* Correspondence: adebambo@physics.unaab.edu.ng (P.O.A.); stephane.kenmoe@uni-due.de (S.K.); adebayo@physics.unaab.edu.ng (G.A.A.)

Abstract: The density functional theory was used to explore the structural, electronic, dynamical, and thermoelectric properties of a VIrSi half-Heusler (HH) alloy. The minimum lattice constant of 5.69 (Å) was obtained for VIrSi alloy. The band structure and the projected density of states for this HH alloy were calculated, and the gap between the valence and conduction bands was noted to be 0.2 eV. In addition, the quasi-harmonic approximation was used to predict the dynamical stability of the VIrSi HH alloy. At 300 K, the Seebeck coefficient of 370 and $-270 \mu\text{V.K}^{-1}$, respectively, was achieved for the p and n-type doping. From the power factor result, the highest peak of $18 \times 10^{11} \text{ W/cm.K}^2$ is obtained in the n-type doping. The Figure of Merit (ZT) result revealed that VIrSi alloy possesses a high ZT at room temperature, which would make VIrSi alloy applicable for thermoelectric performance.

Keywords: phonon dispersion; PDOS; mechanical properties; power factor; figure of merit



Citation: Adebambo, P.O.; Adetunji, B.I.; Uto, O.T.; Kenmoe, S.; Adebayo, G.A. First-Principles Calculations of the Phonon, Mechanical and Thermoelectric Properties of Half-Heusler Alloy VIrSi Alloys. *Crystals* **2022**, *12*, 1838. <https://doi.org/10.3390/cryst12121838>

Academic Editor: Hongbin Bei

Received: 21 November 2022

Accepted: 10 December 2022

Published: 16 December 2022

Publisher's Note: MDPI stays neutral with regard to jurisdictional claims in published maps and institutional affiliations.



Copyright: © 2022 by the authors. Licensee MDPI, Basel, Switzerland. This article is an open access article distributed under the terms and conditions of the Creative Commons Attribution (CC BY) license (<https://creativecommons.org/licenses/by/4.0/>).

1. Introduction

Since the last century, the global demand for energy has considerably expanded. Climate change, which adversely affects the depletion of fossil resources and leads to an energy crisis, is one of the causes of the high demand in energy around the globe. However, experts are attempting to increase the efficiency of environmentally friendly technology such as biomass, solar photovoltaic, wind turbines, and thermoelectric as a way of providing a solution to the problem of high energy demand. Thermoelectric technology which depends on thermoelectric materials (TE) for the conversion of heat into electricity and vice versa is gaining momentum as a potential technology needed to address the problem of high energy demand globally. These materials have attracted extensive research in an effort to meet this technology's demand in recent times [1–3]. A dimensionless figure of merit is typically used to assess a material TE performance. Due to their relatively high Seebeck coefficient, Heusler alloys are among the most promising thermoelectric materials [1–5].

The wide family of Heusler alloys, which Fritz Heusler initially described in 1903, has qualities that can be altered to suit technological applications in numerous fields of science and engineering research. A prominent member of this family is the half-Heusler (HH) alloys [6]. These half-Heusler alloys typically have some distinctive qualities that set them apart from other kinds of Heusler alloys. They typically have 18 valence electrons with a small band gap, which is one of these qualities. By substituting at different crystal locations, it is possible to change the thermoelectric efficiency of half-Heusler compounds and achieve the ideal balance of Seebeck, electric resistivity, and thermal conductivity [7–14]. In turn,

this might lower these alloys lattice thermal conductivity and raise their power factor, making them become ideal for thermoelectric applications.

Numerous researchers have looked into the thermoelectric properties of various half-Heusler compounds in the past and in the present using both experimental and theoretical techniques. For instance, due to their Figure of Merit of 0.7 [12,13], the half-Heusler alloys $MNiSn$ ($M = Ti, Zr, \text{ and } Hf$) have been touted as one of the promising materials for thermoelectric technology. Here, they replace Ni with Pd in a methodical way such that solid-state reactions can be used to create the samples. High-quality component powder is heated for 96–168 h in a flowing argon atmosphere to 1173 K. $FeXSb$ ($X = V, Nb$) has also been reported to have a high power factor and Seebeck coefficient at room temperature [15–18]. For these materials, X-ray diffraction (XRD) was used on a RigakuD/MAX-2550PC diffractometer to identify the samples' phase structures. The samples have no impurity phases, according to the XRD examination.

In order to calculate the structural, electrical, elastic, and thermoelectric properties of novel $HfPtPb$ HH alloys, Kaur and Rai recently used density functional theory with semi-classical Boltzmann transport equations under the constant relaxation time approach. This alloy is mechanically and dynamically stable, according to their report. Additionally, it was discovered that for this material, the n-type doping produced the maximum Seebeck coefficient. Within an enhanced TB-mBJ potential, Wang and Wang used first-principles simulations to examine the electronic structure and thermoelectric characteristics of half-Heusler semiconductors $ABPb$ ($A = Hf, Zr; B = Ni, Pd$) [19]. Using Boltzmann transport theory, they calculated Seebeck and power factor within the constant relaxation time as well as projected the band structure for both p- and n-type doped compounds. According to their findings, all of the compounds are semiconductors with a narrow band gap. Additionally, they stated that their power factors closely match the outcomes of the experiment and offered some suggestions for improving the thermoelectric properties.

The ternary intermetallic full- and half-Heusler alloys have stoichiometric compositions of X_2YZ and XYZ , respectively. These classifications are made such that the X and Y elements are transition metals, while the Z elements are semiconductor or sp atoms. Nevertheless, our choice of $VIrSi$ alloy conforms with this arrangement. However, we have carefully noted that only a little work had been conducted on this alloy. Furthermore, the high thermoelectric properties that usually characterize the undoped HH alloys is one of the motivations to explore additional research on HH compounds. To our knowledge, one of such compounds is $VIrSi$ alloy, for which extensive investigations, including the calculation of structural, electronic, elastic, dynamical, and thermoelectric properties, are scarce. Consequently, we have used the density functional theory as well as semi-classical Boltzmann transport theory within the constant rigid band approximation to investigate the structural, mechanical, electrical, and thermoelectric properties of $VIrSi$ alloy.

2. Computational Procedure

The pseudopotential plane wave method within density functional theory, as implemented in the Quantum Espresso simulation code [20,21], was used to calculate the structural and electrical properties of this alloy. The exchange correlation functional was approximated using the Generalized Gradient Approximation (GGA) [22] with Perdew–Burke–Ernzerhof (PBE). The kinetic energy cut-off of 40 Ry was adopted for this calculation, while a $6 \times 6 \times 6$ grid in the Monkhorst–Pack [23] scheme was constructed for the electronic structure calculation. In order to confirm the convergence of the results, we set a 10^{-4} Ry criterion for convergence of the total energy. The plane wave pseudopotential (PWPP) basis sets which consist of the $3d^2 4s^2, 3s^2 3p^2$, and $5d^7 6s^2$ states for V, Si, and Ir, respectively, were used for all these calculations. Meanwhile, a denser k-point mesh of $(12 \times 12 \times 12)$ grid was used to calculate the electronic density of states (DOS) with a tetrahedra occupation switched on. By fitting the results of the total energy computation to the Birch–Murnaghan equation of states, we were able to extract the majority of the pertinent information concerning the structural behavior of the alloys [24,25]. The quasi-harmonic

Debye model as implemented in the Thermo_pw code [26] was employed to obtain the elastic constant of this alloy. Thereafter, we use the elastic constants to obtain the bulk and shear moduli as given below.

$$B = \frac{C_{11} + 2C_{12}}{3} \quad (1)$$

$$G = \frac{G_V + G_R}{2}. \quad (2)$$

In this case, the upper bound of the G values called the Voigt's shear modulus is represented by the G_V , while Reuss's shear modulus accounting lower bound is denoted by the G_R . We determined G_R and G_V [27–29] as shown in the equations below:

$$G_V = \frac{C_{11} - C_{12} + 3C_{44}}{5}. \quad (3)$$

$$\frac{5}{G_R} = \frac{4}{C_{11} - C_{12}} + \frac{3}{C_{44}}. \quad (4)$$

Meanwhile, the Young's modulus E can be evaluated using:

$$E = \frac{9GB}{G + 3B}. \quad (5)$$

We obtained the Poisson's ratio ν as given below:

$$\nu = \frac{1}{2} \left[\frac{B - \frac{2}{3}G}{B + \frac{1}{3}G} \right]. \quad (6)$$

In addition, we deduced the elastic anisotropy using the relation below:

$$A_e = \frac{2c_{44}}{c_{11} - c_{12}}. \quad (7)$$

We, respectively, calculated the band structure-dependent properties such as the electrical conductivity and thermal conductivity using the equations below:

$$\sigma = ne\mu \quad (8)$$

$$K = K_e + K_l \quad (9)$$

where e is the electronic charge, μ is the mobility, while K_e and K_l represent the electronic and lattice thermal conductivity, respectively. Finally, the power factor and dimensionless Figure of Merit were obtained as shown below:

$$PF = S^2\sigma \quad (10)$$

$$Z_T = \frac{S^2\sigma T}{K} \quad (11)$$

where S , σ , K and T stand for the Seebeck coefficient, electrical conductivity, total thermal conductivity, and absolute operating temperature.

3. Results and Discussion

3.1. Structural and Electronic Properties

We carried out a number of self-consistent computations in order to optimize the crystal structure of VIrSi half-Heusler alloys. This alloy is known to crystallize in $C1_b$ structure with space group $F43m$, where Si atoms are placed at the 0.00 0.00 0.00 position. The Ir atom is located at 0.25 0.25 0.25, and the V atom occupies the atomic position 0.50 0.50 0.50 in the crystal, as shown in Figure 1a. From here, we can see that each V atom is placed in between the Si atoms at the edges. At the same time, Ir atoms are bonded

by both the Si and V atoms. In Figure 1b, the total energy of VIrSi alloys as a function of lattice parameters within the GGA approximations is shown. These lattice parameters were also fitted in Murnaghan's equation of state (EOS), and the results were also plotted along with the calculated lattice parameters in Figure 1b. In addition, we used the fitted in Murnaghan's equation of state (EOS) minimum lattice constant a , bulk modulus B_0 and its pressure derivatives B'_0 for this alloy, and these results are tabulated in Table 1.

The band structure and projected density of state (PDOS) of VIrSi alloys are presented in Figure 2. The dotted line in Figure 2a at 0 eV is the Fermi energy level which separates the valence band from the conduction band. This band structure is depicted along the high symmetry points $\Gamma \rightarrow X \rightarrow W \rightarrow K \rightarrow \Gamma \rightarrow L \rightarrow U \rightarrow W \rightarrow L \rightarrow U$. From here, we notice that the upper valence band is located at W, while the lower conduction band is at X. Consequently, VIrSi alloys have a narrow indirect bandgap of 0.2 eV. The origin of this bandgap in the half-Heusler 18 valence electrons has previously been provided in detail by Galanakis et al. [30]. This energy bandgap corroborates with the results of the PDOS presented in Figure 2b. It is seen from this PDOS calculation that Iridium s and d-orbitals contributed to both the conduction and valence bands. The contribution of the silicon s-orbital and the contribution of the vanadium p-orbital is not well pronounced in both conduction and valence bands.

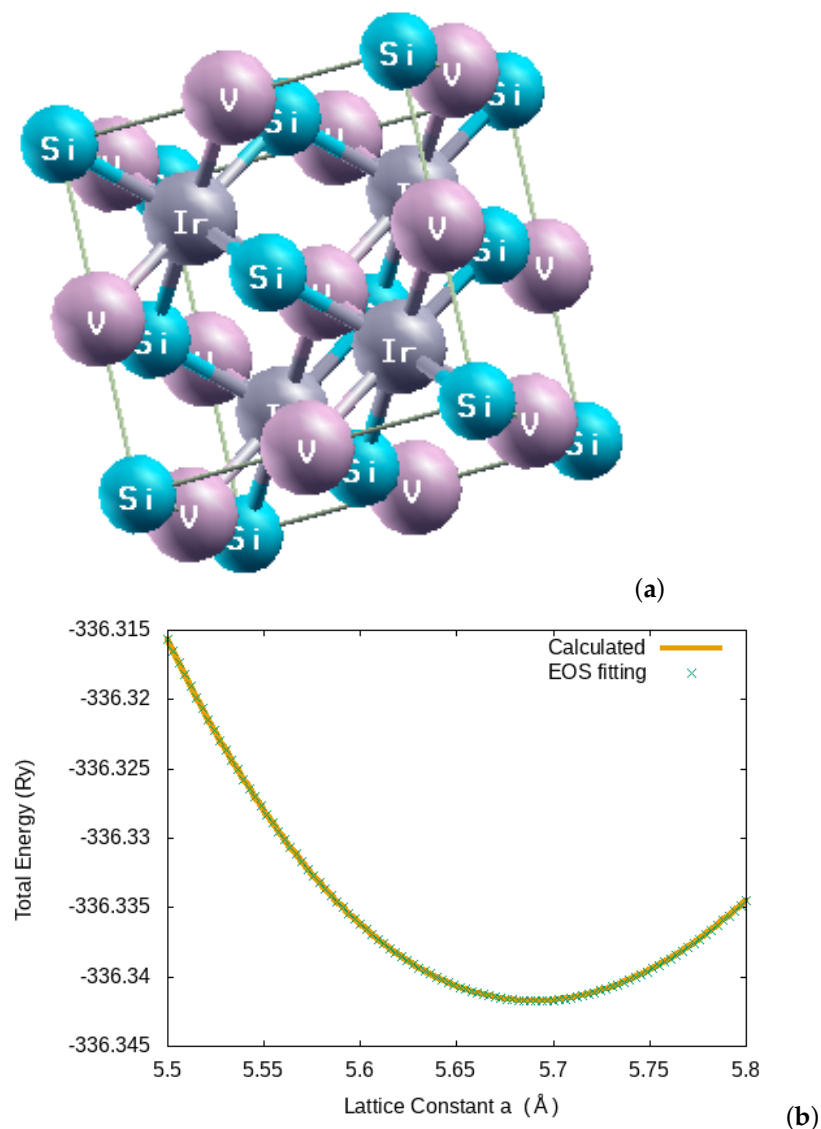


Figure 1. (a) The crystal structure and (b) optimization of the lattice parameters of VIrSi half-Heusler alloy.

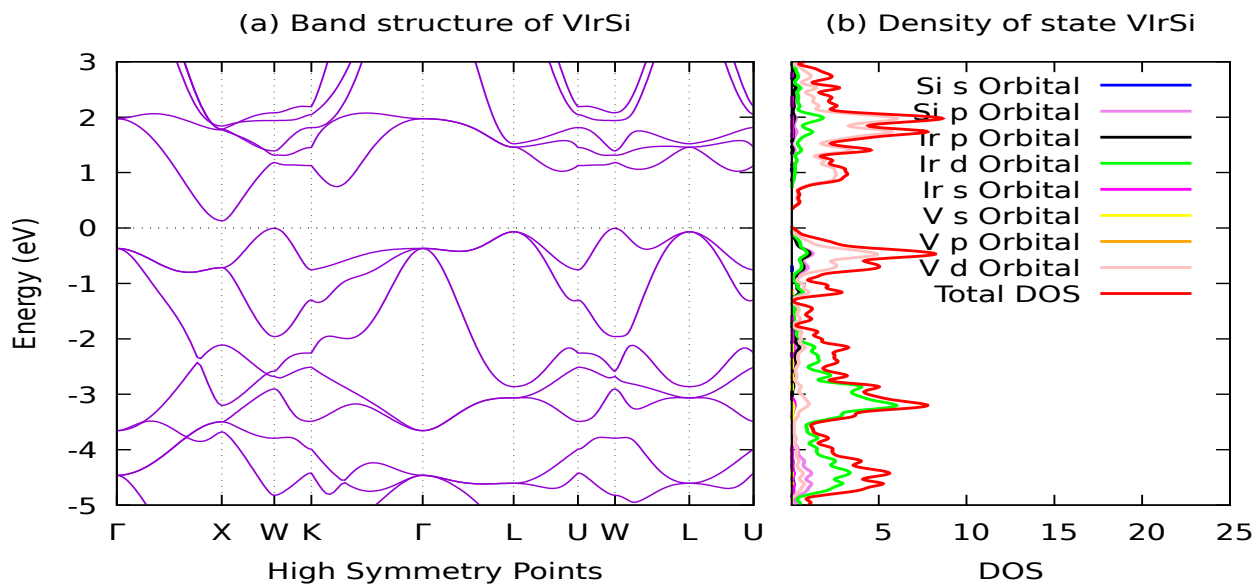


Figure 2. Electronic band structure and projected density of state of VIrSi.

Table 1. Optimization of lattice parameter a , bulk modulus B , and pressure derivative of bulk modulus B' of VIrSi.

Materials	Methods	a (Å)	B (GPa)	B'
VIrSi	Present Work	5.69	218.3	4.22
	Experiment	-	-	-

3.2. Phonon Dispersion Curve of VIrSi Half-Heusler Alloys

The phonon dispersion curves along the Brillouin zone $K \rightarrow \Gamma \rightarrow L \rightarrow U \rightarrow \Gamma \rightarrow W \rightarrow X \rightarrow \Gamma$ path were generated using Phonopy code [31,32] within the quasi-harmonic approximation [33] and are displayed in Figure 3. The dispersion in Figure 3 can be classified into the upper (optical) and lower (acoustic) modes. The acoustic modes lie in between 0 and 5.70 THz, while the optical mode extends from 6.93 to 11.38 THz as also shown in blue in the phonon PDOS in Figure 3b. Both the optical and acoustic branches are separated. The former shows three acoustic modes, while the latter, which contains both the longitudinal optical (LO) and transverse optical (TO) modes, shows three branches for each of them. Our calculated phonon frequencies values are 9.43 THz for LO (Γ) and 7.68 THz for TO (Γ). In the acoustic branch, the calculated longitudinal acoustic is found to be 5.65 THz, while the transverse acoustic is obtained to be 3.90 THz. In the optical mode, which is predominantly dominated by the states V ($Z = 23$) and Si ($Z = 14$), we observed splitting at the Γ point. At the same time, the state of the heavier atom Ir ($Z = 77$) is placed in the acoustic modes of the spectrum. The absence of negative frequency in Figure 3 implies that VIrSi alloy is dynamically stable.

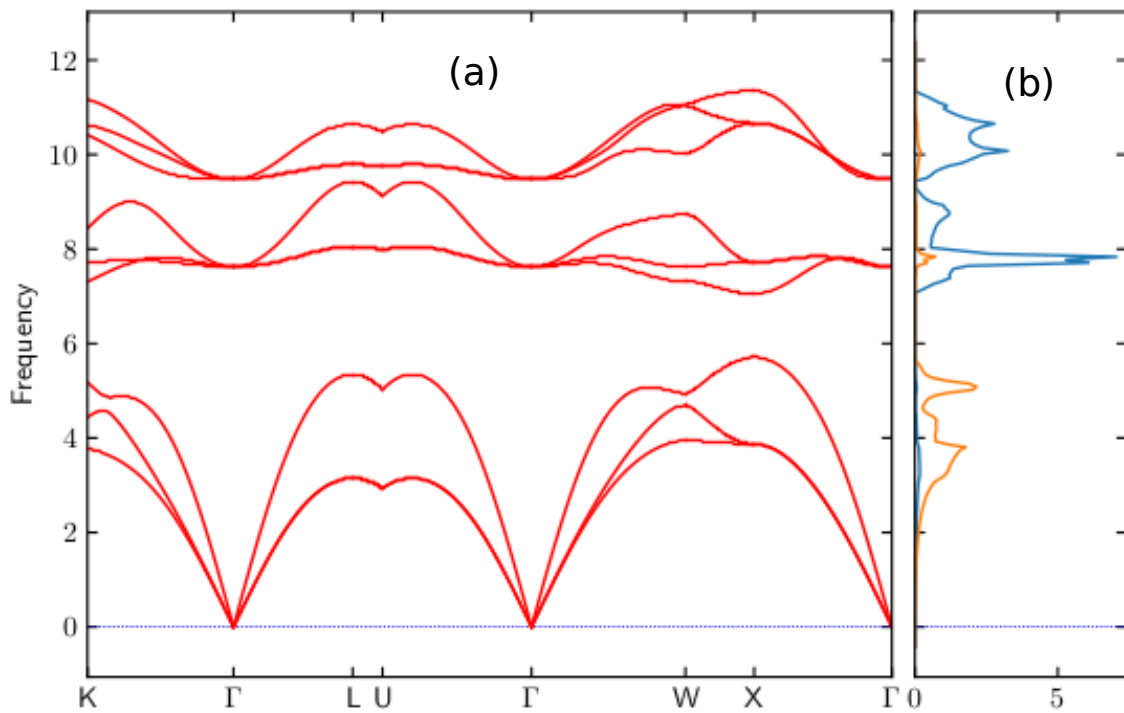


Figure 3. Calculated phonon dispersion curve in (THz) (a) and Phonon DOS (b) of VIrSi alloy.

3.3. Mechanical Properties

The elastic constants, C_{ij} , are critical characteristics for understanding the mechanical behavior of stressed materials because they offer information about the binding between neighboring atomic planes, the anisotropic nature of binding, stiffness, and structural stability. The elastic constants for a cubic system, C_{ij} , are reduced into three independent elastic constants C_{11} , C_{12} , and C_{44} , as shown in equ. 10. The calculated elastic constants C_{11} , C_{12} , and C_{44} , shear modulus (G), ratio of B/G , Young's modulus (E), Poisson's ratio ν , Zener anisotropy factor (A), density (ρ), longitudinal elastic wave velocities (v_l), transverse elastic wave velocities (v_t), average acoustic velocity (v_m), and Debye temperature (θ_D) of VIrSi are listed in Table 2. To our knowledge, there is no experimental or theoretical result regarding the elastic constants of this alloy. Hence, our results can be considered purely predictive. However, our calculated Bulk modulus from EOS (Table 1) is in agreement with one obtained from the quasi-harmonic Debye model as reported in Table 2. The mechanical stability of VIrSi cubic crystals at equilibrium was examined according to the Born and Huang stability criteria [34] as follows:

$$C_{11} > 0, C_{44} > 0, C_{11} - C_{12} > 0, \text{ and } C_{11} + 2C_{12} > 0. \quad (12)$$

Table 2. Elastic constant and elastic moduli of VIrSi.

	C_{11} (GPa)	C_{12} (GPa)	C_{44} (GPa)	G (GPa)	B (GPa)	E (Gpa)	Pugh Ratio	Poisson Ratio	Zener Anisotropy	Debye Temp. (K)
This work	295.02	180.10	109.13	84.36	218.43	224.17	2.589	0.2768	1.899	391.94

The calculated elastic constants satisfy the aforementioned criteria for mechanical stability, showing that this compound is mechanically stable. Pugh proposed an approximation criterion based on the B/G ratio to anticipate the brittle and ductile behavior of materials [35]. If $B/G < 1.75$, the material is considered to be ductile; if $B/G > 1.75$,

the material is said to be brittle [6]. According to the data in Table 2, the B/G ratio of VIrSi HH alloys is 2.589, indicating that VIrSi HH alloy is ductile.

Poisson's ratio indicates the degree of directionality of the covalent bonds in any material. If the critical value of Poisson's ratio is 0.25, then the bonds are said to be non-central, whereas values between 0.25 and 0.50 indicate the presence of central forces [6]. Thus, according to the calculated Poisson's ratio of 0.3285, the VIrSi alloy suggested that interatomic forces are key factors of the central forces. When Hooke's law held true, Young's modulus (E) defined the stress–strain ratio. It is a property that describes a material's stiffness. The value of E indicates the stiffness of the material. As indicated in Table 2, our HH alloy is rigid. In addition, based on the Zener anisotropy factor, our calculated Zener anisotropy factor [36] (1.899) indicates that VIrSi Heusler alloy is elastically anisotropic.

3.4. Thermoelectric Properties of VIrSi Half-Heusler Alloys

In Figure 4a, the power factor variation with energy at different temperatures is clearly depicted. This power factor shows the performance of VIrSi as a thermoelectric material. The maximum value of the power factor is obtained at $18 \times 10^{11} \text{ W/cm.K}^2.\text{s}$ for the n-type doping at 800 K. Meanwhile, for the p-type doping $6 \times 10^{11} \text{ W/cm.K}^2.\text{s}$, the maximum power factor is noted to be also at 800 K. Meanwhile, at 300 K, the maximum power factor of $4 \times 10^{11} \text{ W/cm.K}^2.\text{s}$ and $2 \times 10^{11} \text{ W/cm.K}^2.\text{s}$ were noted for n-type and p-type, respectively.

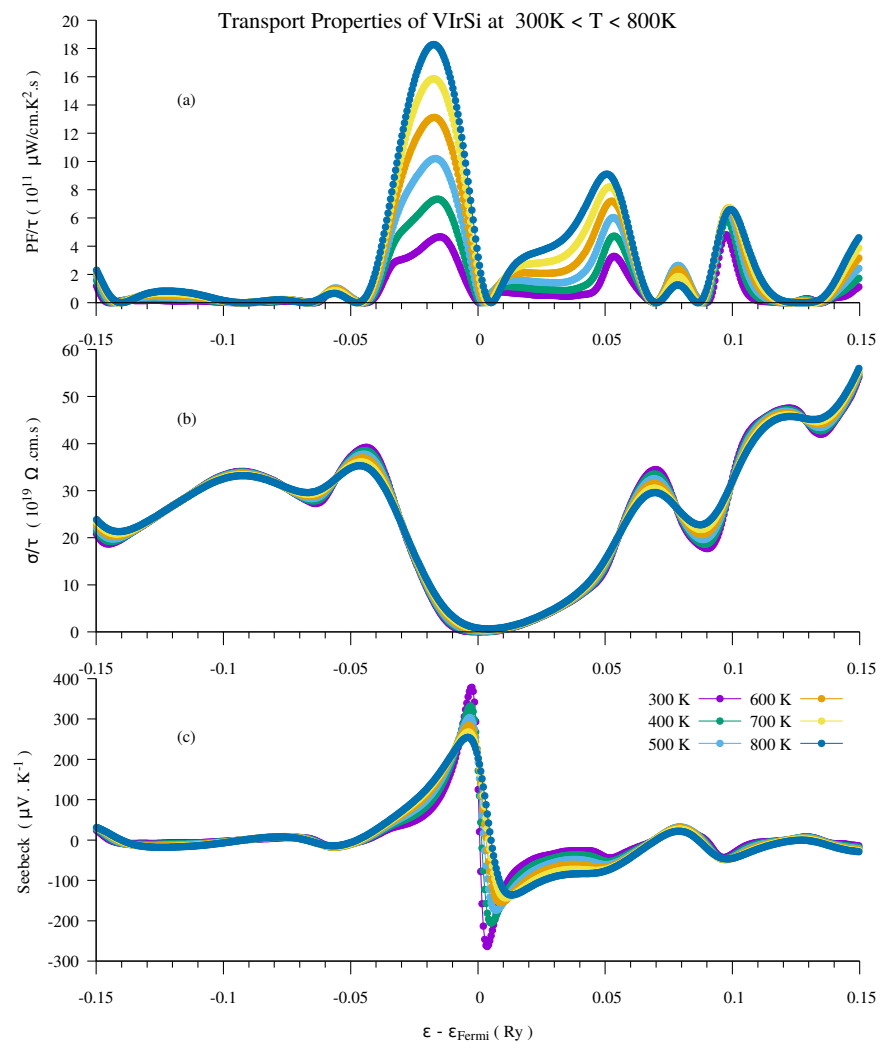


Figure 4. (a) Power factor, (b) Electrical conductivity, and (c) Seebeck coefficient of VIrSi half-Heusler alloys.

Figure 4b presented the variation in electrical conductivity per relaxation time as a function of energy and temperature. At all temperatures, the electrical conductivity per relaxation time exhibits a consistent pattern. Electrical conductivity per relaxation time has a greater gradient for positively increasing energies than for more negative energies. Thus, n-type compositions have a lower electrical conductivity than p-type compositions. Electrical conductivity per relaxation time is zero in the energy range -0.005 to $+0.005$. However, the value grows beyond this range.

As shown in Figure 4c, the Seebeck coefficient at the doping of p-type and n-type materials first increased as the energy increased before reaching a maximum value and decreased drastically as it can be seen from the peaks in the energy range of -0.005 and $+0.005$. The curves intend to be at zero outside this range. The peak maximum for the p-type doping of VIrSi alloy is found at $370 \mu\text{V.K}^{-1}$, while the peak maximum for the n-type doping is observed at $-270 \mu\text{V.K}^{-1}$. The peaks are observed at room temperature, indicating that VIrSi alloy has an excellent thermoelectric trait. The peaks heights tend to be reduced as the temperature rises. The present calculated values of the Seebeck coefficient of VIrSi alloys at 300 K were compared with other half-Heusler alloys VruSb ($+262.67$ and approx. $270 \mu\text{V.K}^{-1}$), NbRuSb (199.88 and approx. $290 \mu\text{V.K}^{-1}$) and TaRuSb (181.5 and approx. $240 \mu\text{V.K}^{-1}$) [37,38]. We conclude that VIrSi has the highest value of the Seebeck coefficient in this regard.

In Figure 5, the dimensionless Figure of Merit is plotted against the chemical potential at each temperature. It is puzzling that even at room temperature, VIrSi possesses a high Figure of Merit, $ZT \approx 0.8$ in the n-type and ≈ 0.68 in the p-type compound. We observe a decrease in the value of ZT as temperature increases, and we attribute this to the strong effects of phonon contribution to the thermal conductivity κ .

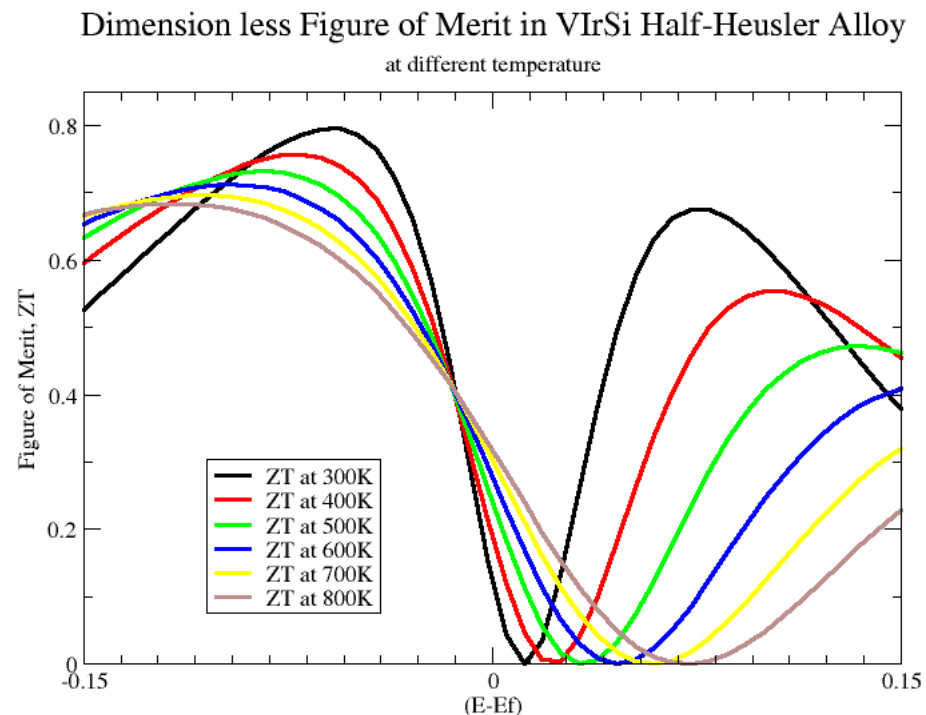


Figure 5. High Figure of Merit in VIrSi half-Heusler alloys from 300 to 800 K.

4. Conclusions

We used the density functional theory and semi-classical Boltzmann transport theory under the constant rigid band approximation to predict the structural, electrical, dynamic, and thermoelectric properties of VIrSi alloy in order to have more insight into these properties. For this alloy, we calculated a lattice constant of 5.69 (\AA) . The band structure and the

projected density of the state of VIrSi alloys were also reported in this work. The contributions of Iridium s and d-orbitals is significant both the conduction and valence bands. In addition, we found that the optical and acoustic branches are separated in the phonon dispersion curve, while the absence of negative frequency in the phonon dispersion curve implies that VIrSi alloy is dynamical stable. To measure the thermoelectric performance of VIrSi alloy, we calculated the Seebeck coefficient, electrical conductivity, the power factor and the dimensionless Figure of Merit. At room temperature, the peak maximum obtained from the calculated Seebeck coefficient is $370 \mu\text{V.K}^{-1}$ for the p-type doping, while $-270 \mu\text{V.K}^{-1}$ is deduced from the n-type doping. Additionally, our findings indicate that n-type compositions have a lower electrical conductivity than p-type compositions. In addition, the power factor of $4 \times 10^{11} \text{ W/cm.K}^2.\text{s}$ was obtained for the n-type doping, while PF of $2 \times 10^{11} \text{ W/cm.K}^2.\text{s}$ was also achieved for p-type doping at room temperature, which implies that VIrSi alloy can be applicable for thermoelectricity. In addition, the high values of both the n- and p-type VIrSi is an indication of its applicability as a power generator.

Author Contributions: Conceptualization, G.A.A. and P.O.A.; methodology, G.A.A., P.O.A.; validation, O.T.U., B.I.A., P.O.A., S.K. and G.A.A.; writing—P.O.A., S.K. and G.A.A.; writing—review and editing, P.O.A., S.K. and G.A.A.; supervision, G.A.A. and S.K.; project administration, G.A.A., P.O.A. and S.K.; funding acquisition, S.K. All authors have read and agreed to the published version of the manuscript.

Funding: Stephane Kenmoe gratefully acknowledges the Deutsche Forschungsgemeinschaft (DFG, German Research Foundation) for the funding 388390466–TRR 247.

Data Availability Statement: Not applicable.

Acknowledgments: SK gratefully acknowledges the Deutsche Forschungsgemeinschaft (DFG, German Research Foundation)—388390466—TRR 247 (2018). Three of us, POA, BIA and GAA, acknowledge support of CINECA for computational facilities under the Project HPC-EUROPA3 (INFRAIA-2016-1-730897), with the support of the EC Research Innovation Action under the H2020 Programme.

Conflicts of Interest: The authors declare no conflict of interest.

References

1. Rowe, D.M. *CRC Handbook of Thermoelectrics*; CRC Press: Boca Raton, FL, USA, 1995. [\[CrossRef\]](#)
2. Kanatzidis, M.G. Nanostructured thermoelectrics: The new paradigm. *Chem. Mater.* **2010**, *22*, 648–659. [\[CrossRef\]](#)
3. Zheng, X.F.; Liu, C.X.; Yan, Y.Y.; Wang, Q. A review of thermoelectrics research – Recent developments and potentials for sustainable and renewable energy applications. *Renew. Sustain. Energy Rev.* **2014**, *32*, 486. [\[CrossRef\]](#)
4. Nolas, G.S.; Poon, J.; Kanatzidis, M. Recent Developments in Bulk Thermoelectric Materials. *MRS Bull.* **2006**, *31*, 199. [\[CrossRef\]](#)
5. Zhao, L.D.; Dravid, V.P.; Kanatzidis, M.G. The panoramic approach to high performance thermoelectrics. *Energy Environ. Sci.* **2014**, *7*, 251–268. [\[CrossRef\]](#)
6. Uto, O.T.; Adebambo, P.O.; Akinlami, J.O.; Kenmoe, S.; Adebayo, G.A. Electronic, Structural, Mechanical, and Thermodynamic Properties of CoYSb (Y = Cr, Mo, W) Half-Heusler Compounds as Potential Spintronic Materials. *Solids* **2022**, *3*, 22–33. [\[CrossRef\]](#)
7. Shutoh, N.; Sakurada, S. Thermoelectric properties of the $\text{Ti}_x(\text{Zr}_{0.5}\text{Hf}_{0.5})_{1-x}\text{NiSn}$ half-Heusler compounds. *J. Alloys Compd.* **2005**, *389*, 204. [\[CrossRef\]](#)
8. Culp, S.R.; Poon, S.J.; Hickman, N.; Tritt, T.M.; Blumm, J. Effect of substitutions on the thermoelectric figure of merit of half-Heusler phases at 800 °C. *Appl. Phys. Lett.* **2006**, *88*, 042106. [\[CrossRef\]](#)
9. Kim, S.W.; Kimura, Y.; Mishima, Y. High temperature thermoelectric properties of TiNiSn-based half-Heusler compounds. *Intermetallics* **2007**, *15*, 349. [\[CrossRef\]](#)
10. Katsuyama, S.; Matsuo, R.; Ito, M. Thermoelectric properties of half-Heusler alloys $\text{Zr}_{1-x}\text{Y}_x\text{NiSn}_{1-y}\text{Sb}_y$. *J. Alloys Compd.* **2007**, *428*, 262. [\[CrossRef\]](#)
11. Sakurada, S.; Shutoh, N. Effect of Ti substitution on the thermoelectric properties of (Zr,Hf)NiSn half-Heusler compounds. *Appl. Phys. Lett.* **2005**, *86*, 3159. [\[CrossRef\]](#)
12. Yu, C.; Zhu, T.J.; Shi, R.Z.; Zhang, Y.; Zhao, X.B.; He, J. High-performance half-Heusler thermoelectric materials $\text{Hf}_{1-x}\text{Zr}_x\text{NiSn}_{1-y}\text{Sb}_y$ prepared by levitation melting and spark plasma sintering. *Acta Mater.* **2009**, *57*, 2757–2764. [\[CrossRef\]](#)
13. Shen, Q.; Chen, L.; Goto, T.; Hirai, T.; Yang, J.; Meisner, G.P.; Uher, C. Effects of partial substitution of Ni by Pd on the thermoelectric properties of ZrNiSn-based half-Heusler compounds. *Appl. Phys. Lett.* **2001**, *79*, 4165–4167. [\[CrossRef\]](#)
14. Zhang, H.; Wang, Y.; Dahal, K.; Mao, J.; Huang, L.; Zhang, Q.; Ren, Z. Thermoelectric properties of n-type half-Heusler compounds $(\text{Hf}_{0.25}\text{Zr}_{0.75})_{1-x}\text{Nb}_x\text{NiSn}$. *Acta Mater.* **2016**, *113*, 41–47. [\[CrossRef\]](#)

15. Fu, C.G.; Xie, H.H.; Liu, Y.T.; Zhu, T.J.; Xie, J.; Zhao, X.B. Thermoelectric properties of FeVSb half-Heusler compounds by levitation melting and spark plasma sintering. *Intermetallics* **2013**, *32*, 39. [[CrossRef](#)]
16. Fu, C.G.; Xie, H.H.; Zhu, T.J.; Xie, J.; Zhao, X.B. Enhanced phonon scattering by mass and strain field fluctuations in Nb substituted FeVSb half-Heusler thermoelectric materials. *J. Appl. Phys.* **2012**, *112*, 124915. [[CrossRef](#)]
17. Fu, C.G.; Zhu, T.J.; Pei, Y.Z.; Xie, H.H.; Wang, H.; Snyder, G.J.; Liu, Y.; Liu, Y.T.; Zhao, X.B. High band degeneracy contributing to high thermoelectric performance in p-type half-Heusler compounds. *Adv. Energy Mater.* **2014**, 1400600. [[CrossRef](#)]
18. Fu, C.G.; Liu, Y.T.; Xie, H.H.; Liu, X.; Zhao, X.; Jeffrey, S.G.; Xie, J.; Zhu, T. Electron and phonon transport in Co-doped FeV_{0.6}Nb_{0.4}Sb half-Heusler thermoelectric materials. *J. Appl. Phys.* **2013**, *114*, 134905. [[CrossRef](#)]
19. Wang, G.; Wang, D. Electronic structure and thermoelectric properties of Pb-based half-Heusler compounds: ABPb (A = Hf, Zr; B = Ni, Pd). *J. Alloys Compd.* **2016**, *682*, 375–380. [[CrossRef](#)]
20. Giannozzi, P.; Baroni, S.; Bonini, N.; Calandra, M.; Car, R.; Cavazzoni, C.; Ceresoli, D.; Chiarotti, G.L.; Cococcioni, M.; Dabo, I.; et al. QUANTUM ESPRESSO: A modular and open-source software project for quantum simulations of materials. *J. Phys. Condens. Matter* **2009**, *21*, 395502. [[CrossRef](#)]
21. Giannozzi, P.; Andreussi, O.; Brumme, T.; Bunau, O.; Nardelli, M.B.; Calandra, M.; Car, R.; Cavazzoni, C.; Ceresoli, D.; Cococcioni, M.; et al. Advanced capabilities for materials modelling with Quantum ESPRESSO. *J. Phys. Condens. Matter* **2017**, *29*, 465901. [[CrossRef](#)]
22. Perdew, J.P.; Burke, K.; Ernzerhof, M. Generalized Gradient Approximation Made Simple. *Phys. Rev. Lett.* **1996**, *77*, 3865. [[CrossRef](#)]
23. Monkhorst, H.J.; Pack, J.D. Special points for Brillouin-zone integrations. *Phys. Rev. B* **1976**, *13*, 5188. [[CrossRef](#)]
24. Birch, F. Finite Elastic Strain of Cubic Crystals. *Phys. Rev.* **1947**, *71*, 809. [[CrossRef](#)]
25. Murnaghan, F.D. The Compressibility of Media under Extreme Pressures. *Proc. Natl. Acad. Sci. USA* **1944**, *30*, 244. [[CrossRef](#)] [[PubMed](#)]
26. Dal Corso, A. Elastic constants of beryllium: A first-principles investigation. *J. Phys. Condens. Matter* **2016**, *28*, 075401. [[CrossRef](#)] [[PubMed](#)]
27. Voigt, W. Lehrbuch der Kristallphysik (B. B. Teubner, Leipzig, 1928). 2022, p. 739. Available online: <https://www.worldcat.org/title/lehrbuch-der-kristallphysik-mit-ausschluss-der-kristalloptik/oclc/23322264> (accessed on 21 November 2022).
28. Hill, R. The Elastic Behaviour of a Crystalline Aggregate. *Proc. Phys. Soc. (Lond.)* **1952**, *65*, 349. [[CrossRef](#)]
29. Huntington, H.B. The Elastic Constants of Crystals. *Solid State Phys.* **1958**, *7*, 213–351.
30. Galanakis, I.; Dederichs, P.H.; Papanikolaou, N. Slater-Pauling behavior and origin of the half-metallicity of the full-Heusler alloys. *Phys. Rev. B* **2002**, *66*, 174429. [[CrossRef](#)]
31. Togo, A. Phonopy. Available online: <http://phonopy.sourceforge.net/> (accessed on 22 November 2018).
32. Matsumoto, A.; Koyama, Y.; Togo, A.; Choi, M.; Tanaka, I. Electronic structures of dynamically stable As₂O₃, Sb₂O₃, and Bi₂O₃ crystal polymorphs. *Phys. Rev. B* **2011**, *83*, 214110. [[CrossRef](#)]
33. Wallace, D.C. *Thermodynamics of Crystals*; Dover Publications: Mineola, NY, USA, 1998.
34. Born, M.; Huang, K. *Dynamical Theory of Crystal Lattices*; Oxford Clarendon Press: Oxford, UK, 1956; pp. 120–156.
35. Pugh, S.F. Relations between the Elastic Moduli and the Plastic Properties of Polycrystalline Pure Metals. *Lond. Edinb. Dublin Philos. Mag. J. Sci.* **1954**, *45*, 823. [[CrossRef](#)]
36. Zener, C. *Elasticity and Anelasticity of Metals*; University of Chicago Press: Chicago, IL, USA, 1948.
37. Kaur, K.; Rai, D.P.; Thapa, R.K.; Srivastava, S.; Structural, electronic, mechanical, and thermoelectric properties of a novel half Heusler compound HfPtPb. *J. Appl. Phys.* **2017**, *122*, 045110. [[CrossRef](#)]
38. Fang, T.; Zheng, S.; Zhou, T.; Yan, L.; Zhang, P. Computational prediction of high thermoelectric performance in p-type half-Heusler compounds with low band effective mass. *Phys. Chem. Chem. Phys.* **2017**, *19*, 4411. [[CrossRef](#)] [[PubMed](#)]